

Direct visualisation of underwater phenomena in soil-fluid interaction and analysis of the effects of an ambient pressure drop on unsaturated media

Visualisation directe des phénomènes sous-marins concernant l'interaction sol-fluide et analyse des effets d'une chute de pression ambiante sur les milieux insaturés

H.J. KÖHLER, *Bundesanstalt für Wasserbau, Karlsruhe, Germany*

M.A. KOENDERS, *Kingston University, Kingston on Thames, UK*

ABSTRACT

A description is given of an apparatus in which a wide range of hydraulic conditions can be realised. A unique observation system using optical fibre based 'endoscopes' and an imaging system that includes a significant digital processing element enables the visualisation of grain and fluid motion as well as air bubble behaviour in granular deposits of specified composition and geometry under externally imposed hydraulic conditions. Examples are given and a particular application in which a soil is studied that is fluidized by an external pressure drop. A description of the fluidized behaviour is given and the outcomes are cast in terms of a mathematical/physical model for fluidized material. This model is then used to predict the extent of a fluidized region in a one-dimensional situation.

RÉSUMÉ

On donne ici la description d'un appareil qui permet de réaliser un large éventail de conditions hydrauliques. Un système unique d'observation employant des 'endoscopes' à fibre optique et un capteur d'image incluant une part importante de traitement numérique, permet de visualiser le mouvement des grains et du fluide ainsi que le comportement des bulles d'air dans des dépôts granulaires de composition et de géométrie données, sous l'effet de conditions hydrauliques imposées. Des exemples sont donnés ainsi qu'une application particulière dans laquelle on étudie un sol qui est fluidisé par une chute de pression externe. Une description du comportement fluidisé est donnée et les résultats sont présentés en termes de modèle physico-mathématique pour un matériau fluidisé. Ce modèle est alors utilisé pour prévoir l'extension d'une région fluidisée dans une situation unidimensionnelle.

1. Introduction

An apparatus in which fluid flow phenomena in a granular environment can be studied is described below, as well as a novel visualisation methodology, which enables detailed tracking of soil particles, fluid particles and small air bubbles. The apparatus is different from the ones usually employed in hydraulics studies, such as the wave flume, in that the interest is not focused on obtaining the (scaled) flow field for a given structural option, but rather boundary conditions are imposed directly in a laboratory controlled manner. The precise way in which this is done is outlined in the next section; it must however be said from the outset that the apparatus is designed in such a way that a substantial range of external pressures and flow controls – both static and cyclic – can be achieved – sufficient to study most practical hydraulic civil engineering conditions, with the possible exception of earthquake loading conditions. Moreover a static external effective stress can be imposed and work is under way to make this programmable time dependent as well.

The apparatus works then as a large cell in which a certain granular environment is created – for example a geotechnical base/filter structure. The performance of the granular contents under hydraulic loading is monitored by means of an endoscopic method. Selected pores are illuminated by guiding light to a chosen position using an optical fibre. A second optical fibre, encased in a small metal box with a window is inserted in the cell to reveal the mo-

tion of fluid and soil particles in a particular pore. The dimensions of the metal box are chosen in such a way that no significant interference with the water flow occurs. The motion is recorded with a video camera and an image processing method analogous to traffic flow analysis is used to make quantitative measurements.

The measurement system so installed enables the study of phenomena that take place in the granular subsoil. This in turn makes it possible to ascertain the validity of physical/mathematical models in which the mode of motion of either fluid or solid particles is postulated. Previously such motion could only be studied at the surface of a transparent cell wall, either by laser-Doppler methods [1], laser-speckle methods [2] or direct visual observation [3]. It is also relevant to mention the study of particle motion by using glass particles and an oily fluid of the same refractive index [4], [5]. The method put forward here measures particle motion directly and fluid motion by employing a fine particulate tracer. This is further discussed in the next section. In addition to the optical measurement system a conventional system is in place to monitor average pore pressures at different locations.

An intriguing phenomenon that takes place in the subsoil is the expansion and contraction of small gas bubbles due to fluctuating external pressures, for example meteorological variation in the air pressure or pressure variation induced by waves created by shipping activity. It transpires that where the average water depth in a practical setting is insufficient to cause the gas bubbles to col-

Revision received June 28, 2002. Open for discussion till June 30, 2003.

lapse – and this is nearly always the case where water depths are less than some 20 metres – micro currents associated with the inflation and deflation of these bubbles may cause significant particulate motion if effective stresses are small. This form of erosion has hardly ever been reported before and as such the observation of this mechanism is one of the results of the use of the apparatus and associated measurement methodology.

The structure of this paper is as follows. First the mechanical details of the apparatus are given and the optical and image processing systems are described. Then recorded images for one chosen set of boundary conditions are shown and the motion revealed in these is discussed. Finally the implications of the observations of the behaviour of air bubbles in subsoil are calculated and made relevant to the propensity for erosion processes in unprotected waterways.

2. Experimental

The apparatus is sketched in Figure 1a and a photograph is shown in Figure 1b. It consists of a large pressure tank with floor area measurements $2.0 \times 0.8 \text{ m}^2$ and a height of 0.80 m. The walls are ribbed to avoid spurious deformation; these have been tested to perform satisfactorily in this respect for pressures not exceeding 4 Bar. The tank is entirely sealed, using rubber seals around the lid of the apparatus. To test the quality of the sealant a water-

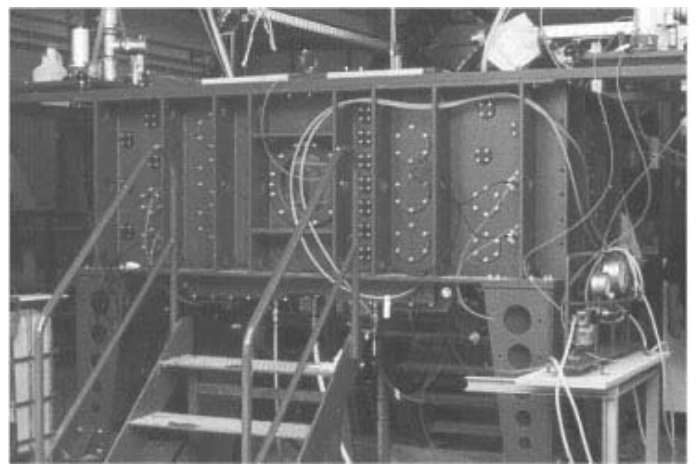


Fig. 1b Photograph of the apparatus, viewed from the side.

filled tank, again pressurised to 4 Bar, displayed no significant loss of pressure over a period of up to four days.

The tank is filled with layers of soil by pouring a tapping. The porosity of each layer is controlled by weight and volume measurements. Different types of soil may be coloured for easy identification. After the soil has been put in place the tank is closed using the sealed lid. The soil need not fill the tank completely; when an artificial top load is required the lid is made to rest on the soil, but open water conditions are created by omitting the lid. Any top load that is required is applied via a system of four pistons that exert pressure as homogeneously as possible; the pistons are driven by air pressure and their action may be programmed to simulate oscillating top load conditions.

A horizontal water flow – the main longitudinal component – inside the tank is controlled by a closed system water current loop that enters the tank via a pressure chamber in which a honeycomb structure is present to dampen any flow fluctuations. The effectiveness of this system is such that fluctuations in pressure come to less than 20 cm for a head of 1.40 m. To add to the versatility of the operating conditions the pressure chambers are normally partitioned into three sections (extendible to ten sections) in order to create a stratified flow. Again the horizontal flow is programmable to satisfy a particular time schedule.

Another extension of the possible flow regimes is the imposition of a transverse flow component, which is applied in a similar manner as the longitudinal flow. A system of hinges is further envisaged to enable a shearing effective stress in the longitudinal direction, but this is as yet not operative. A further feature of the loading conditions is that the overall water pressure can be varied according to a timed programme and in this way external pressure variations are simulated.

The apparatus is thus able to handle conditions relevant to a wide range of civil engineering flow/stress configurations: filtration problems in unsteady hydraulic conditions (for example the ones that occur in the vicinity of coastal protective structures), river bed erosion problems, navigable canal loading and suffusion effects near broad rivers. Furthermore a range of problems associated with strong stratification effects and alien inclusions can be studied, in particular the ones due to near-impervious layers require detailed investigation.

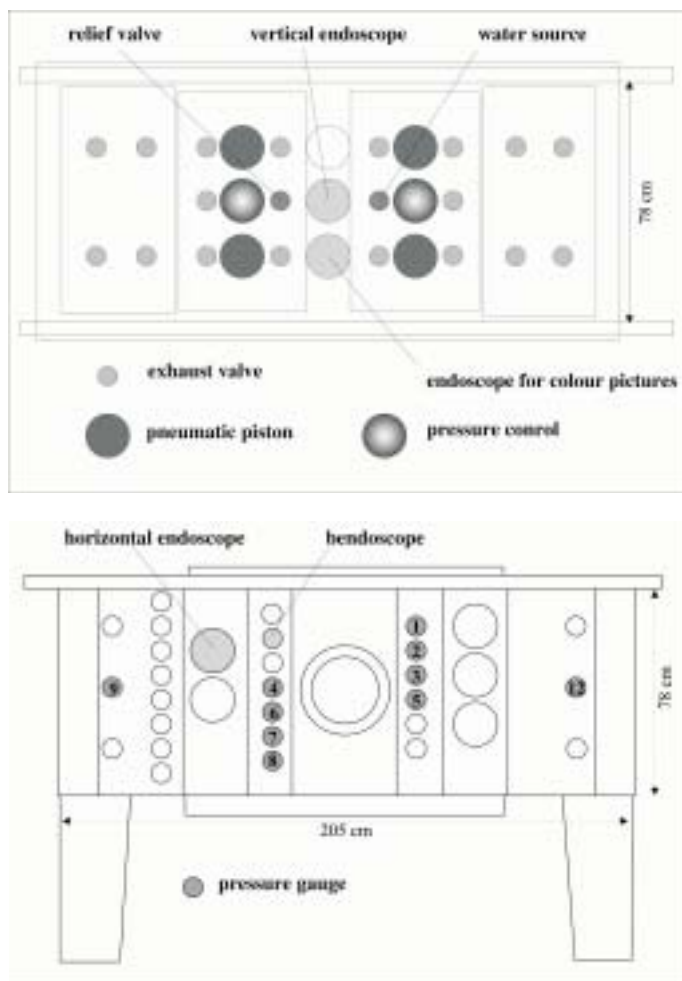


Fig. 1a Sketch of the apparatus: (top) top view, (bottom) side view.

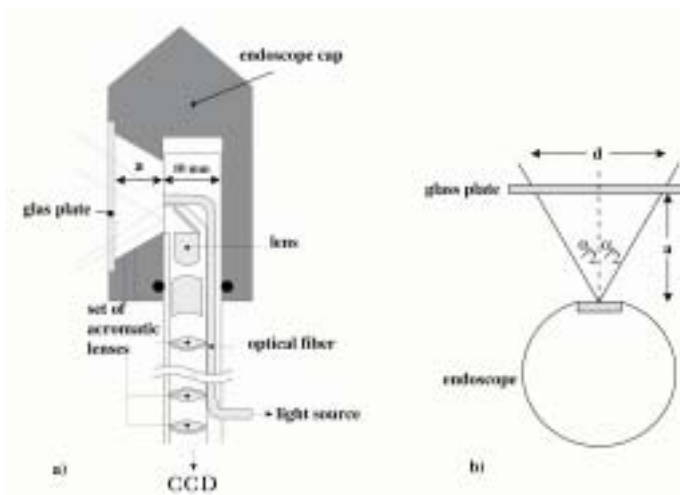


Fig. 2 Cross sectional view of the endoscope viewing system and optics.

As mentioned in the Introduction, the study of the motion of both the fluid and the particles is carried out using an endoscopic technique, see Figure 2. This technique works as follows. White light is introduced via an optical fibre of 1mm thickness. (An alternative method consists in one based on a local LED device to introduce the light). At the same time another optical fibre for viewing purposes is inserted. The pair of fibres is guided through either a rigid or a flexible endoscope. The latter contains a viewing window. The endoscope diameters range from 4 mm to 10 mm. Typically they operate in gravel of a similar size so that the disturbance to the flow is nugatory. The viewing window ranges in size from $6 \times 6 \text{ mm}^2$ to $2 \times 2 \text{ mm}^2$. An achromatic lens is used to magnify the image by up to a factor of two. The maximum size of the observed region depends on the aperture angle of the endoscope; typically it has a radius of the order of some 5 mm. The optical field depth is of the order of 2-3 mm.

Images are obtained by video camera at the end of the viewing fibre. The images are stored on an analogue laser video recorder. The image sampling rate is 25 Hertz; each image contains 25×25 pixels.

Conventional piezo-electric pressure gauges (Transinstruments, 4000K series) are installed to monitor the fluid pressure throughout the tank on a continuous basis. A typical set-up contains three endoscopes and some 15 pressure gauges. A substantial amount of data is thus collected and needs processing.

3. Data collection and image processing

The process of the analysis of the data is now outlined. The signals from the pressure gauges are interpreted in the usual manner. The images from the endoscopes can either be used directly or may be given special treatment. For the latter a vast array of image processing software is available in order to improve the rather rough image quality and also to perform automatic detection of motion. As the images are collected in digital form it is relatively easy to perform processing procedures, for example to improve the contrast. However, it must be pointed out that image processing is no longer in its infancy and quite sophisticated software can

be employed with a view to obtaining information of considerable detail concerning the fluid and particulate flow fields in the field of vision at any given time.

Two types of operations are distinguished in the digital processing methodology. The first consists of operations on a *single image*, the second is carried out on a *sequence of images*. Operations on single images include the homogenization of the illumination in the observed field; this operation is necessary to correct for the very unequal light quality that is inevitably associated with the photography of shadowy objects. Contrast improvement is done to emphasise more clearly the location of particulate material and also distinct air bubbles. The latter process can be taken further by using an algorithm called 'edge detection'. Finally colours can be assigned to certain areas of a specific greyness in the image. Alternatively – where images are taken at different colours – these can be 'translated' into a map with a pre-selected number of distinct colours. All these methods are described in the image processing literature: [6], [7], [8], [9], [10].

Operations on a sequence of images are obviously designed to determine flow fields. It is important in this case to identify particular objects that have shifted position in going from one image to the next. Software to do this automatically has been developed for various purposes, for example traffic analysis. It must be pointed out that these few brief sentences pertain to an enormous body of computer code. Extensive reporting on this topic has been done and is still continuing, see [11], [12], [13]. In addition to pre-existing software special algorithms have been developed for this particular application; these include algorithms to detect simultaneous translation and rotation of irregular objects and associated object identification. The latter problem is especially involved because no predefined particle shape can be assumed, and – to add to the complexity of the problem – only two dimensional images are extracted from the photography, so that the three dimensional information must be inferred in some way. Recent literature on this topic is [14], [15], [16] and naturally this subject is not being developed in isolation, but many other disciplines make use of its findings.

Illustrations of the image processing system are provided below in graphical format.

4. Example of flow field in a pore

The apparatus and measurement method can be employed to determine the flow field in a pore in a gravel bed. The measurements described below refer strictly to low Reynolds number flows, though there may be a small transient effect. A horizontal flow field is established as described in Section 2. In order to measure the flow field, a pore is instrumented with an endoscope of size smaller than the grainsize, so that no significant interference with the fluid flow pattern in the vicinity of the pore is to be expected. The flow field is derived from the motion of small tracer particles, which are dispersed in the pressure chambers at the inlet of the tank. The particles are silt grains with an average diameter of $40 \mu\text{m}$. To determine the velocity of the particles, images are taken at a frequency of 25 Hz.

The result is shown in Figure 3 for one pore. The light during one

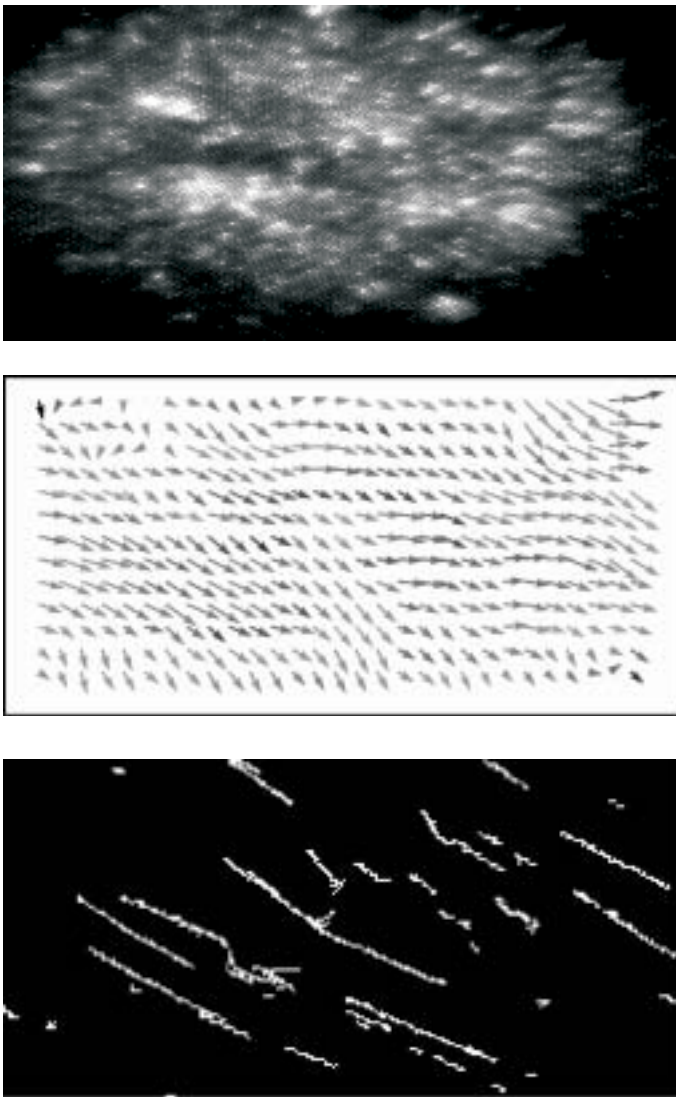


Fig. 3 Images from slow fluid flow in a pore in a gravel bed. (a) Light from a single image as it is dispersed from tracer particles; (b) the Eulerian field of motion; (c) stream paths derived from the velocity field (Lagrange).

exposure of a duration of 1.2 seconds is shown in Figure 3a. The result of a succession of images processed to yield the velocity vector field is shown in Figure 3b. The stream paths derived from the vector field are demonstrated in Figure 3c. Other quantities such as various velocity gradients can also be derived but are not shown here. The method is calibrated to give absolute values, see [14].

The potential for this measurement method is to determine statistical information about the fluid velocity in a number of pores; in this way the distribution of velocity throughout the packed bed can be ascertained. The effect on the distribution at different average fluid velocities can also be found. This is not followed up here; the flow measurement is only included by way of illustration.

5. Effects due to ambient pressure change

It is easy to detect small gas bubbles in the soil using the endoscopic technique. An illustration is shown in Figure 4. These bub-

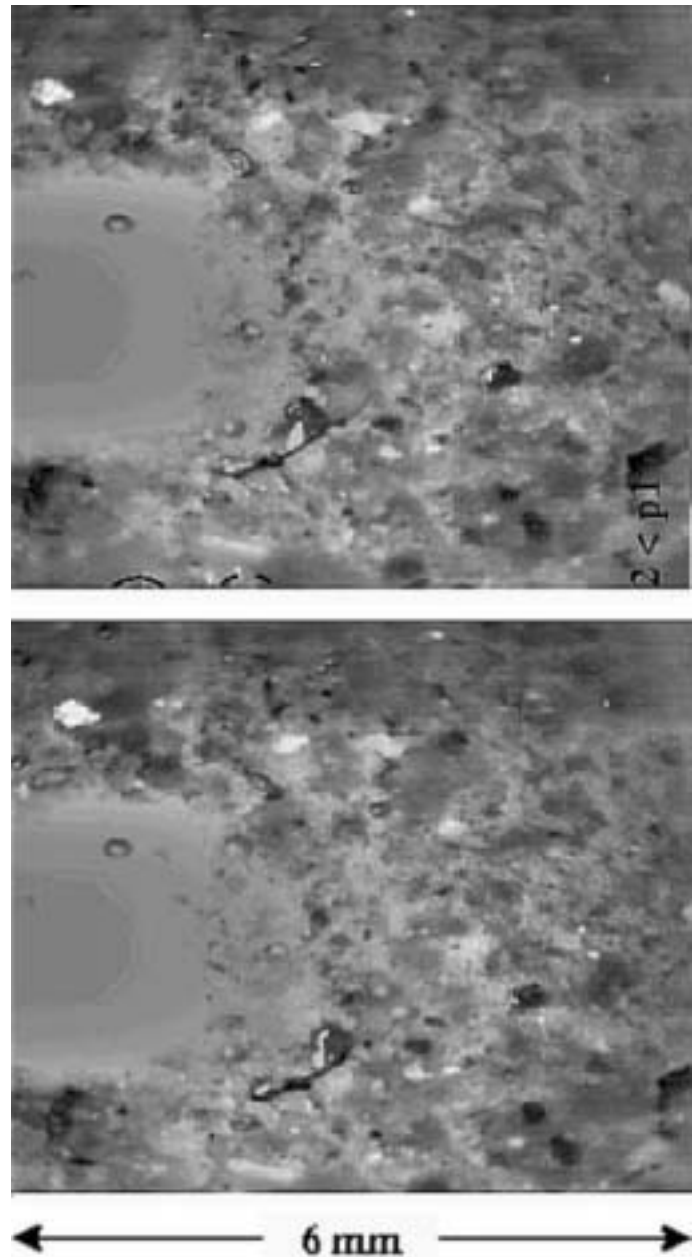


Fig. 4 Image of air bubbles that adhere to surrounding grains in a fluid. The air bubbles are recognised as deeply black features with shining reflections at the top. Two are clearly seen at the centre, slightly to the left of the pictures. They inflate as the the ambient pressure is decreased. (a): at pressure p_1 ; (b): at pressure $p_2 < p_1$.

bles adhere to the surrounding grains and if the ambient pressure is changed they expand or contract. Figures 4 a, b show two stages of the same pore with air bubbles inflated after a pressure decrease. In common engineering practice soil testing it is quite common to make a great effort to reduce the amount of gas in the fluid. This is done for the good reason that the presence of the air distorts the volume expansion measurement necessary to determine the soil response. However, the purpose here is different: gas is a natural constituent of riverbeds and packed beds at shallow depths and it is of interest to see how they behave.

Primarily it is noted that it is very difficult to get rid of air bubbles. Only at very high pressures do they 'pop' and in most shal-

low, practical applications such pressures never occur. Secondly, it must be kept in mind that gas bubbles are often created by local bacterial activity – not necessarily restricted to ‘swampy’ conditions. They are part of the engineering reality then and their behaviour must be accounted for.

The compressibility of a gas bubble depends on the local average pressure. The latter increases with depth and therefore the volume variation due to an externally imposed pressure variation is depth dependent. The differential volume change leads to a micro flow, which is generally in the vertical direction and where the pressure gradient exceeds the skeletal stress, fluidization effects may occur. A mathematical analysis of this erosion phenomenon is given below. Experimental proof of the reality of the effect is now discussed.

Figure 5 a and b show two images of the same region in a particle/fluid/gas mixture. The grains have been given a colour: a red layer lies underneath a green layer and the location of the endoscope is just at the boundary of the two layers. By means of contrast enhancement the two regions – red and green – are here made visible as two distinctly different shades of grey. There is no difference in the granular composition of the layers. The initial layer separation is in the region where fluidization effects are expected. In Figure 5 b the ambient pressure has been reduced (as can be seen from the inflated air bubbles). It is also observed that the grains have moved: more red grains are higher than in Figure 5a and some green grains have moved down. Thus mixing has taken place, which is really only possible in a fluidized state. It is also observed that two of the bubbles have coalesced, testimony to both their persistence and non-static nature. The degree of saturation in these experiments is equivalent to what may be expected in practical circumstances (some 85-95%), but the magnitude of the pressure drop, as well as the drop time, have been exaggerated for demonstration purposes. The drop here amounts to over two metres in less than 20 seconds; these are figures associated only with the motion of large ships. Even if the drop is much smaller (and takes longer to establish), such as pressure fluctuations of meteorological origin or natural water level fluctuations, there may well be a fluidized region if no skeletal stress is present. Substantial erosion may then occur if, in addition to the pressure fluctuations, there exists a superficial flow and designed bed protection may be required.

The phenomena that occur during a pressure drop have been studied by means of a video recording of the endoscope view. The behaviour during fluidization of a packed bed is best described as an orderly, more or less even expansion of the granular matrix, accompanied by some diffusive differential motion between the grains. The latter phenomenon naturally implies that there are regions that hardly deform at all – the motion is nonhomogeneous. No abrupt motion is seen however; the effect that is sometimes called ‘boiling’ – which is mostly associated with the phenomenon of fluid-driven particulate material into an open surface – is definitely absent. But large volume strains are a definite feature. These observations are helpful when modelling the fluidization behaviour. Below this is done for a simple system where no top load is present. The analysis yields estimates for the extent of the fluidized region, which in turn may be used to estimate the

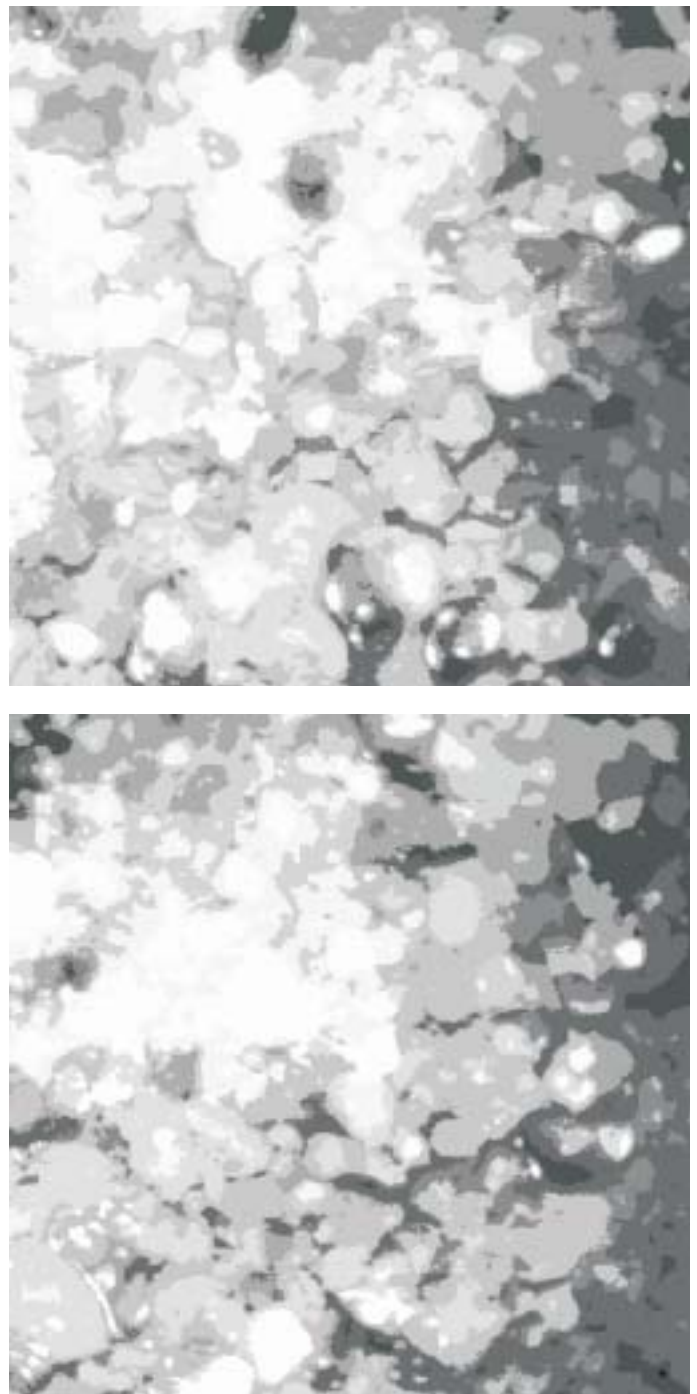


Fig. 5 Dyed grains; (a) initially separate, (b) mixed when the bed is fluidized due to a pressure drop and the presence of air bubbles. The grains have been coloured red and green. The latter show up in these grey-scale images as the bright (white areas). The former are light grey. Air bubbles show as shiny black smooth features with a shiny spot. Three can be clearly distinguished in the bottom right of (b). Grains have moved position as a result of the general motion in the packed bed.

amount of erosion that may potentially take place.

6. Mathematical model of consolidation during fluidization

The consolidation phenomena that take place during an externally imposed pressure drop are now modelled mathematically. The constitutive behaviour of a soil/fluid/gas mixture has been studied

in the past. Most effects that are relevant are discussed by Teunissen [17], drawing on earlier work by Barends [18]. These authors have demonstrated that for bubbles beyond a certain diameter (roughly 10 μm at atmospheric conditions), the compressibility β' of a gas/fluid mixture can be approximated and expressed in the gas solubility ω , the initial saturation s_i , the actual fluid pressure p_t and the initial pressure p_i :

$$\beta' = \frac{1}{p_t} - \frac{(1-\omega)s_i}{p_i + (1-\omega)s_i(p_t - p_i)} \quad (1)$$

The parameter ω is always small compared to 1, typically in the order of 0.02. For small variations from the initial pressure the compressibility satisfies:

$$\beta' = \frac{1-s_i}{p_i} \quad (2)$$

Thus an estimate of the initial pressure and the initial saturation are required to be able to model the compressibility of the fluid/gas mixture and hence of the consolidation effects that follow an increase or decrease in the external pressure. The latter is described by Biot's Equation [19], relating the soil permeability k , the porosity n and the skeletal volume strain e . For a homogeneous soil in a fluid with specific weight γ_w and for one dimensional problems, Biot's Equation gives a differential equation for the excess pore water pressure p :

$$\frac{k}{\gamma_w} \frac{\partial^2 p}{\partial x^2} = n\beta' \frac{\partial p}{\partial t} + \frac{\partial e}{\partial t} \quad (3)$$

Various corrections to this equation have been put forward. These are all discussed by Barends [18]. One significant correction pertains to free moving gas bubbles; this correction appears not to be relevant as gas bubbles are nearly always observed to stick to the soil particles.

The compressibility depends on the ambient pressure p_i , which consists of the atmospheric pressure at the fluid surface p_0 and a term that depends on the water depth. The latter varies according to the water depth according to $\gamma_w x$, where x is measured downwards from the top of the water level.

An expression for e for *densely packed material under compressive stress* is obtained from a deformation modulus F , such that the excess skeletal stress $\sigma' = Fe$. Using furthermore Terzaghi's stress principle relating total stress excess σ , the excess porewater pressure p and the skeletal stress (using the convention that compressive stresses are negative) such that $\sigma = \sigma' - p$, the rate of change of the volume strain is seen to be:

$$\frac{\partial e}{\partial t} = \frac{1}{F} \left(\frac{\partial \sigma}{\partial t} + \frac{\partial p}{\partial t} \right) \quad (4)$$

The total stress satisfies stress equilibrium in one dimension and is thus independent of the spatial co-ordinate x , while its time dependence is prescribed by the external loading programme. The

analysis here is intended for small variations in the external fluid pressure, due to changing water levels.

The relevant equation that requires solution is:

$$\frac{k}{\gamma_w} \frac{\partial^2 p}{\partial x^2} = \left[\frac{n(1-s_i)}{p_0 + \gamma_w x} + \frac{1}{F} \right] \frac{\partial p}{\partial t} + \frac{1}{F} \frac{\partial \sigma}{\partial t} \quad (5)$$

The soil occupies a region $x > x_0$, where x_0 is the water depth. F is assumed to be a constant in the densely packed soil. The saturation s_i is also assumed to be a constant, independent of depth.

A complication in the analysis is that *fluidization* occurs. For fluidized material the stress-strain behaviour outlined in the previous paragraphs is incorrect: the elastic moduli collapse and the only skeletal stress that can still be transmitted via the grains is associated with a strain rate: $\sigma' = f \partial e / \partial t$, where f is a viscous modulus. A combined analysis, incorporating both elastic and strain dependence, is pursued here to demonstrate the effects that take place. The skeletal stress at any point is:

$$\sigma' = Fe + f \frac{\partial e}{\partial t} \quad (6)$$

A Laplace transform with Laplace frequency λ is applied give:

$$\hat{\sigma}' = F\hat{e} + f(\lambda\hat{e} - e(0)) \quad (7)$$

Again Terzaghi's principle is applied and \hat{e} is solved:

$$\hat{e} = \frac{\hat{\sigma}' + \hat{p} + fe(0)}{F + \lambda f} \quad (8)$$

Substitution in Equation (3) gives:

$$\frac{k}{\gamma_w} \frac{\partial^2 \hat{p}}{\partial x^2} = \frac{n(1-s_i)}{p_0 + \gamma_w x} (\lambda\hat{p} - p(0)) + \frac{\lambda(\hat{\sigma}' + \hat{p} + fe(0))}{F + \lambda f} - e(0) \quad (9)$$

To make further progress something about the behaviour of f must be ascertained. Now the observations from the previous section are used as a guide.

The order of magnitude of the parameter f is estimated by letting it be proportional to the fluid viscosity μ and inversely proportional to the relative gap width between particles h/\bar{a} , where \bar{a} is the particle radius. An estimate for the relative gap width for densely packed spheres of equal radius at solidosity $\phi = 1-n$ is given by Torquato et al [20]:

$$\frac{h}{\bar{a}} = \frac{(1-\phi)^3}{6\phi(2-\phi)} \quad (10)$$

Thus the order of magnitude of f is:

$$f \approx \frac{6\mu\phi(2-\phi)}{(1-\phi)^3} \quad (11)$$

Typically, at the porosity expected in soil, the ratio a/h is in the

order of magnitude of 100. Thus the parameter f is estimated to be of the order of magnitude of $0.1 \text{ Nm}^{-2}\text{s}$ in water. The underlying assumptions of this analysis require seriously amendment in that no account is taken of grain to grain interaction, which contributes significantly to the energy loss in any differential motion for a relatively densely packed material. It is therefore necessary to emphasise that the estimate – equation (11) – pertains to a *well-fluidized material* only. For partially fluidized materials the particulates form aggregates of N particles. The gap width is more or less the same as for a homogeneously fluidized material, but the relative gap width is reduced by a factor of N , thus increasing the overall viscosity by a factor of N . For materials on the edge of fluidization $N \rightarrow \infty$, for well-fluidized material $N = 1$. As fluidization becomes established N is reduced due to the successive disintegration of particle conglomerates. The reduction in N is accompanied by a substantial expansive volume strain.

A time scale τ is introduced in order to compare the viscous behaviour with estimates for the skeleton stiffness at low effective stress F and the water/gas stiffness β'^{-1} . A typical value for F is in the order of magnitude of 10^8 Nm^{-2} . β'^{-1} at atmospheric pressure and 90% saturation is of the order of 10^6 Nm^{-2} . For the effects of viscosity, as expressed by f , to be in the same order of magnitude as these two figures requires a time scale of $\tau N^{-1} \approx 10^{-7}\text{s}$. To bring this time scale in line with a practical time scale, a value of N of some 10^6 is required. This is not as large a number as it would appear: in a linear dimension it represents about 100 particles. Assuming particles of a diameter of $100 \mu\text{m}$, a typical conglomerate will have a diameter in the order of 1 cm. This is an awkward length scale to observe: laboratory tests are usually on the scale of ten times this value, while endoscopic observation has a field size of approximately one tenth of this value. Numerical simulations of particle assemblies usually apply to 10^3 - 10^4 particles. However, in a fully fluidized material ($N = 1$) the viscous behaviour would always dominate. For a material at the onset of fluidization, where the packing is still very dense, and for materials in which a compressive stress – no matter how small – is present, the fluid/gas compressibility dominates the deformation behaviour at the saturation and ambient pressure milieu envisaged here.

Fluidization takes place when the vertical gradient exceeds the unit weight of the soil, Terzaghi [21]. The unit weight is called γ and the fluidization criterion for the ‘critical gradient’ i_c , directly expressed as a fraction of the unit weight of water, reads:

$$i_c = \frac{1}{\gamma_w} \frac{\partial p}{\partial x} = (1-n) \frac{\gamma}{\gamma_w} \quad (12)$$

A practical value is of the order of magnitude of 1.

With these considerations in mind equation (5) is further analysed. When the medium is unfluidized, or only just fluidized so that no or little volume strain has taken place yet, it is reasonable to put:

$$\frac{k}{\gamma_w} \frac{\partial^2 \hat{p}}{\partial x^2} = \frac{n(1-s_i)}{p_0 + \gamma_w x} \lambda \hat{p} + \frac{\lambda(\hat{\sigma} + \hat{p})}{F} \quad (13)$$

Fluidization takes place from the top of the granular deposit. At the top the pressure boundary condition requires that the pressure amplitude equals the ambient pressure modification: $\hat{p}(0) = -\hat{\sigma}$. Thus near the top the pressure amplitude may always be approximated in terms of the gradient amplitude \hat{A} , as:

$$\hat{p}(x) = \hat{A}(x - x_0) - \hat{\sigma} \quad (14)$$

In a region where \hat{A} exceeds the critical gradient fluidization takes place. When this region is sufficiently large, conglomerate break-up will be accompanied by a volume strain and at a time point t_0 there will be region $x_0 < x < x_1$ where F has collapsed and f is reducing. (The boundary x_1 will naturally be time-dependent). The equation that rules the fluidized region for times $t > t_0$ reads:

$$\frac{k}{\gamma_w} \frac{\partial^2 \hat{p}}{\partial x^2} = \frac{n(1-s_i)}{p_0 + \gamma_w x} (\lambda \hat{p} - p(t_0)) + \frac{(\hat{\sigma} + \hat{p})}{f} \quad (15)$$

The rough approximation $\hat{p}(x) = \hat{A}(x - x_0) - \hat{\sigma}$ is used to get an idea of the effect of rate dependence. This linear approximation – which is basically a first order estimate of the time-dependent gradient at the top boundary of the granular deposit – is substituted in equation (15) to give:

$$\begin{aligned} \frac{n(1-s_i)}{p_0 + \gamma_w x_0} (\lambda (\hat{A}(x - x_0) - \hat{\sigma}) - A(t_0)(x - x_0) - \sigma(t_0)) \\ + \frac{\hat{A}(x - x_0)}{f} = 0 \end{aligned} \quad (16)$$

The time span over which the analysis is valid is sufficiently short to let f be constant and $\sigma(t) \approx \sigma(t_0)$. The latter implies that $\hat{\sigma} \approx \sigma(t_0)/\lambda$ and therefore:

$$\frac{n(1-s_i)}{p_0 + \gamma_w x_0} (\lambda \hat{A} - A(t_0)) + \frac{\hat{A}}{f} = 0 \quad (17)$$

The immediate result is:

$$A(t) = A(t_0) \exp \left[\frac{-(p_0 + \gamma_w x_0)t}{fn(1-s_i)} \right] \quad (18)$$

The gradient thus reduces with a time constant approximately equal to $fn(1-s_i)/(p_0 + \gamma_w x_0)$. This time constant becomes very small when f collapses to its single-particle value that corresponds to $N=1$, when it is less than a μs . For a fluidized bed that hangs together in conglomerates of 10^6 particles (roughly corresponding to a linear dimension of 1 cm for sand grains), the time constant is of the order of 0.1 s. This is an indication of the time it takes to restore the gradient to the critical value. (The result justifies the assumption that the external load may be regarded as a constant for the period of time over which the analysis is valid). What this analysis shows then is that when fluidization takes place, driven by phenomena that typically take a time in the order of seconds,

the viscous effects in the medium ensure that the gradient never exceeds the critical value. In physical terms this implies that the soil does not 'boil', but that fluidized effects due to the presence of gas bubbles in the soil take place without any externally visible features. The soil, however, may be in a fluidized state for a substantial period of time – precisely as has been observed in the experiments.

7. Estimate of the extent of the fluidized zone under ramp loading

The extent of the region prone to fluidization may be estimated from a solution of equation (13) for various types of external loading. A rather practical analytical approximation is put forward in this section, giving an estimate of the extent of the fluidized zone $\delta(t)$, under a ramped reduction of the external water pressure, for times $t \geq t_1$, where t_1 is the time-point at which fluidization first takes place. An estimate for t_1 is given in equation (30). The principal soil properties relevant to the problem are encased in one parameter a , defined as $a^2 = 4n(1 - s_i) / k$. Furthermore parameters $\dot{\sigma}$, the rate of external pressure reduction, and x_0 – the height of the free water level – need to be specified. The analysis is performed as follows. Returning equation (13) to the time domain, a solution is sought of:

$$\frac{k}{\gamma_w} \frac{\partial^2 p}{\partial x^2} = \frac{n(1 - s_i)}{p_0 + \gamma_w x} \frac{\partial p}{\partial t} + \frac{1}{F} \frac{\partial(\sigma + p)}{\partial t} \quad (19)$$

for $x \geq x_1(t)$, the fluidization boundary, under the boundary conditions:

$$p(x_1(t), t) = i_c \gamma_w (x_1(t) - x_0) - \sigma(t); \quad \left. \frac{\partial p(x, t)}{\partial x} \right|_{x=x_1(t)} = i_c \gamma_w \quad (20)$$

Typically the value of F is much greater than p_0 , thus implying that a reasonable approximation is achieved if the term proportional to F^{-1} in equation (19) is neglected for a solution in a region of magnitude $x - x_0 < n(1 - s_i) F \gamma_w^{-1}$. Introducing a spatial variable $y = x + \gamma_w^{-1} p_0$ and Laplace transforming yields:

$$ky \frac{\partial^2 \hat{p}}{\partial y^2} - n(1 - s_i) \lambda \hat{p} = 0 \quad (21)$$

The solution to this equation is well known in terms of the modified Bessel function $K_1(\bullet)$, see Abramowitz and Stegun, Section 9.6 [23]:

$$\hat{p}(y) = \hat{A}(\lambda) \sqrt{y} K_1(a \sqrt{\lambda y}) \quad (22)$$

In formula (22) $\hat{A}(\lambda)$ is a constant which can be determined from the boundary conditions and $a^2 = 4n(1 - s_i) / k$. The Laplace transformed pressure gradient is:

$$\frac{\partial \hat{p}(y)}{\partial y} = -\frac{1}{2} a \hat{A}(\lambda) \sqrt{\lambda} K_0(a \sqrt{\lambda y}) \quad (23)$$

$\hat{A}(\lambda)$ is eliminated from equations (22) and (23) to give:

$$\hat{p}(y) = \frac{-2\sqrt{y}}{a\sqrt{\lambda}} \frac{\partial \hat{p}(y)}{\partial y} \frac{K_1(a\sqrt{\lambda y})}{K_0(a\sqrt{\lambda y})} \quad (24)$$

Use is now made of approximations that are available for the modified Bessel functions for large arguments, that is for large values of λ , or equivalently, small values of the time t :

$K_\nu(z) \approx \sqrt{\pi/(2z)} e^{-z} (1 + (4\nu^2 - 1)/(8z) + O(z^{-2}))$. Practical values for $a\sqrt{\lambda y} > 4$ are appropriate for the problems below and therefore the ratio of the Bessel functions in formula (24) may be approximated as unity. The inverse Laplace transform of the equation is simply:

$$p(y, t) = \frac{-2\sqrt{y}}{a} \int_0^t \frac{1}{\sqrt{\pi(t - \tau)}} \frac{\partial p}{\partial y}(y, \tau) d\tau \quad (25)$$

The result is further developed for ramp loading. Fluidization will take place at a time $t = t_1$, the point when the gradient at the top of the layer reaches the critical value. The boundary conditions follow from equation (20). First define:

$$y_0 = x_0 + \gamma_w^{-1} p_0, \quad y_1(t) = x_1(t) + \gamma_w^{-1} p_0 \quad (26)$$

$$\text{For } t < t_1: \quad p(y_0, t) = -\dot{\sigma}t \quad (27)$$

$$\text{For } t \geq t_1: \quad p(y_1(t), t) = i_c \gamma_w (y_1(t) - y_0) - \dot{\sigma}t; \quad \left. \frac{\partial p(y, t)}{\partial y} \right|_{y=y_1(t)} = i_c \gamma_w \quad (28)$$

Substitution of these conditions in equation (25) leads to the following results:

$$\text{For } t < t_1: \quad \left. \frac{\partial p(y, t)}{\partial y} \right|_{y_0} = \frac{\dot{\sigma}a\sqrt{t}}{\sqrt{\pi y_0}} \quad (29)$$

$$t_1 = \pi y_0 \left(\frac{i_c \gamma_w}{\dot{\sigma}a} \right)^2 \quad (30)$$

For $t \geq t_1$ call the thickness of the fluidized front $\delta(t) = y_1(t) - y_0$; equation (25) is now employed to estimate the thickness of the front $\delta(t)$. The pressure gradient in the point $y_1(t)$ is approximated for values in the vicinity of y_0 in the time intervals $0 < \tau < t_1$ and $t_1 < \tau < t$. The former is found from a spatial Taylor series up to second order using the values given by equation (29) and the differential equation itself, equation (21). The latter is obtained from a second order polynomial in τ using the estimate that is already available for the gradient at the time $\tau = t_1$, the value at time $\tau = t$ – where the value is $i_c \gamma_w$ – and the fact that the time derivative must vanish at the point of fluidization. The latter point is impor-

tant as the main contribution to the integral is in the vicinity of $\tau = t$, so the gradient should be approximated quite accurately in this point. The integrals over τ in equation (25) are easily done and an equation in $\delta(t)$ follows. This equation is solved and the result is depicted in figure (6).

In order to carry out an experimental verification the relevant soil parameters need to be known. The calculation presented here produces a prediction of the excess pore pressure as a function of both position and time. Backfitting this result to the experimental pore pressure data gives a best estimate for the value of a . This parameter is itself composite: $a = \sqrt{4n(1-s_i)/k}$. The permeability k can in principle be obtained independently from either a laboratory test or from an estimate formula, appropriate to the grain size. The degree of saturation is very much an in situ property and virtually impossible to control. The porosity can be estimated with some accuracy. Details of the backfitting procedure are provided in a paper by Roussell et al [23], for a set of data on sand with a measured permeability of 2.0×10^{-4} m/s. The pore pressure data are then consistent with a value for $a \approx 20$ s^{1/2}m^{-1/2}, leaving a saturation of some 95%. The estimated error in a – derived from the variation of the pore pressure profiles – is estimated at some 30%. The onset of fluidization is then detected using the endoscopic evidence as described in Section 5. The time it takes for the first fluidization phenomena to take place is estimated using $\sigma \approx 600$ Pas⁻¹ and $y_0 \approx 2.3$ m. The result is $t_1 \approx 5$ s. The first signs of fluidization are detected

by the endoscope just below the surface (at roughly -1 cm) at some 7 seconds after the pressure drop is initiated. Bearing in mind that in situ determination of the saturation is made difficult by the fact that this quantity may vary by quite a margin from position to position, this is a fair estimate. It is therefore concluded that the analysis gives a very reasonable quantification of the physical processes that occur. The scatter in the data is not due to poor experimentation, but rather the result of naturally occurring fluctuations in the subsoil.

The natural time constant of the problem is $a^2 y_0$; this is the rate at which reconstitution takes place when the ramp load ceases and the load is kept constant. Typically the time constant is in the order of many thousands of seconds and therefore no quick reconstitution will take place, leaving the fluidized region vulnerable to eroding forces.

7. Conclusions

The apparatus described here and its associated measurement technique permit the study of detailed small-scale motion of particles, fluid and air bubbles that take place in a packed bed. The two examples of measurements given are relevant to engineering practice and help to cast light on phenomena that occur in nature. The versatility of the apparatus makes possible various other studies, which will be reported in due course.

The type of study envisaged is typically aimed at acquiring insight in the deformation processes that take place prior to and during erosion. It is not practical to use the apparatus for routine testing. The example of the use of the apparatus and associated measurement/visualisation system given in this paper serve as a practical illustration.

The analysis of the pore pressure development in unsaturated subsoil under an external pressure drop can obviously be extended to include the effects of artificially placed permeable top load and then information about the amount of load required to withstand eroding forces that are characteristic for a specific location can be ascertained. This is clearly a significant engineering application, which is made possible because of the observation of fluidizing material enabled by the apparatus described in this paper.

8. Acknowledgments

Assistance from Dr. H. Haussecker and staff and students at Heidelberg University, Centre for Interdisciplinary Scientific Computing is gratefully acknowledged. HJK is grateful for financial support from the Bundesanstalt für Wasserbau in Karlsruhe.

9. References

- [1] DRAIN, L. E. (1980) *The Laser Doppler technique* John Wiley & Sons, Chichester.
- [2] HINSCH, K. D. (1993) *Particle image velocimetry* in Speckle Metrology (R.S. Sirohi ed). Marcel Dekker, New York, 235-324.
- [3] VAN DYKE, M. (1982) *An album of fluid motion* The Parabolic Press, Stanford Ca.

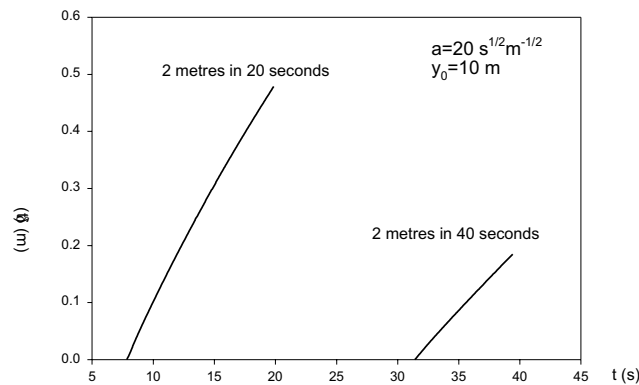
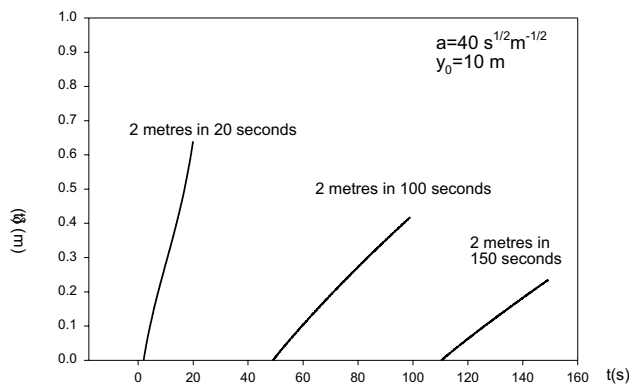


Fig. 6 The extent of a fluidized zone for two values of the parameter a ($a^2 = 4n(1-s_i)/k$) and for various choices of the pressure drop time characteristics.

- [4] KOENDERS, M. A., PATEL, H. S., WILLIAMS, A. F. (1993) 'The description of a filter process as a two-phase flow process' Proc. Geo-filters '92. Karlsruhe, (J. Brauns et al eds) Balkema, Rotterdam, 181-188.
- [5] KOENDERS, M. A. (1998) 'Effects of microstructure and non-linearity in heterogeneous materials' Journal of Physics D. **31** (15), 1875-1882.
- [6] JAEHNE, B. (1991). 'Digital image processing' Springer, Berlin.
- [7] BURT, P. J. (1984) 'The pyramid as a structure for efficient computation. In Multiresolution and Analysis' (A Rosenfeld, ed) Springer series in information sciences, Vol 12, Springer, New York, 6-35.
- [8] RICE, J. A. (1988) 'Mathematical statistics and data analysis' Wadsworth and Brooks/Cole Advanced Books and Software, Pacific Grove, Ca.
- [9] TAGARE, H., DE FIGUEIREDO, R. (1990). 'On the localisation performance measure and optimal edge detection' IEEE Transactions on pattern analysis and machine intelligence, **12** (12), 1186-1190.
- [10] CANNY, J. (1986) 'A computational approach to edge detection' IEEE Transactions on pattern analysis and machine intelligence, **8** (6), 679-698.
- [11] JAEHNE, B. (1993) 'Spatio-temporal image processing, theory and applications' Lecture notes in computer science, Vol 751, Springer, Berlin.
- [12] DUNCAN, J., CHOU, T. (1992). 'On the detection of motion and the computation of optical flow' IEEE Transactions on pattern analysis and machine intelligence, **14**, 346-352.
- [13] AGGARWAL, J. K. (1986) 'Motion and time-varying imagery - an overview' Proceedings workshop on motion: representation and analysis, Charleston, Washington. IEEE Computer Society Press, Los Alamitos Ca., 1-6.
- [14] SPIES, H., BERINGER, O., GROENING, H., HAUSSECKER, H. (1999) 'Analyzing particle movements at soil interfaces', Handbook on computer vision and applications (B. Jähne, H. Haussecker and P. Geissler (eds)). Academic Press, New York.
- [15] JAEHNE, B., HAUSSECKER, H., SPIES, H., SCHMUNDT, D., SCHURR, U. (1998) 'Study of dynamical processes with tensor-based spatio-temporal image processing techniques' Proc. Computer Vision -ECCV '98 Freiburg, Germany, Volume II (H. Burkhardt and B. Neumann, eds.), Springer-Verlag, Berlin, 322 - 336.
- [16] KOEHLER, H. J., HAUSSECKER, H., JAEHNE, B. (1996) 'Detection of particle movements at soil interfaces due to changing hydraulic load conditions, localised by a digital image processing technique' Proc. Géofilters 96, Montréal (J. Laffeur and A.L. Rollin, eds), Bitech Publishers Ltd, Richmond BC., 215-226.
- [17] THEUNISSEN, J. A. M. (1982) 'Mechanics of a fluid-gas mixture in a porous medium' Mechanics of Materials **1**, 229-237.
- [18] BARENDT, F. B. J. (1980) 'Nonlinearity in groundwater flow', Thesis, University of Technology Delft.
- [19] BIOT, M. A. (1941) 'General theory of three dimensional consolidation', J. Appl. Physics, **12**, 155-164.
- [20] TORQUATO, S., LU, B., RUBINSTEIN, K. (1990) 'Nearest-neighbor distribution functions in many-body systems' Phys Rev A, **41** (4), 2059-2074.
- [21] TERZAGHI, K. (1943) 'Theoretical soil mechanics' Wiley, New York.
- [22] ABRAMOWITZ, M., STEGUN, I. A. (1965) 'Handbook of mathematical functions' Dover, New York.
- [23] ROUSSELL, N., KOEHLER, H. J., KOENDERS, M. A. 'Analysis of erosion protection measures in partially saturated subsoils' in Proc. Filters and drainage in geotechnical and environmental engineering (eds Wolski, W. and Mlynarek, J.) Balkema, Rotterdam, 75-82.

List of symbols

a	$\sqrt{4n(1-s_i)}/k$
\bar{a}	particle radius
\hat{A}	hydraulic gradient Laplace amplitude
e	volume strain of the soil skeleton
f	viscous volume modulus
F	volume deformation modulus
h	gap width between particles
i_c	'critical' gradient for fluidization
k	soil permeability
$K_{\nu}(\bullet)$	modified Bessel function of order ν
n	soil porosity
N	number of particles in an aggregate
p	excess pore water pressure
p_0	atmospheric pressure
p_i	initial ambient pressure
p_t	actual total fluid pressure
s_i	initial saturation
t	time
t_0	time point at which the fluidized front has proceeded as far as x_1
t_1	time at which the fluidization first takes place
x	position co-ordinate
x_0	water depth to the top of the soil
x_0	location of the boundary of the fluidized front
y	$x + \gamma_w^{-1} p_0$
y_0	$x_0 + \gamma_w^{-1} p_0$
y_1	$x_1 + \gamma_w^{-1} p_0$
β'	compressibility of gas/fluid mixture
γ	soil unit weight
γ_w	specific weight of the pore water
δ	thickness of the fluidized front
ϕ	solidosity
λ	Laplace frequency
μ	fluid viscosity
σ	total stress
σ'	skeletal stress
$\dot{\sigma}$	rate of external pressure reduction
τ	auxiliary time parameter
ω	gas solubility
\wedge	Laplace transformed variable